Vol. 46, No. 1 (2024) 126-140, DOI: 10.24874/ti.1528.08.23.11

Tribology in Industry

www.tribology.rs

RESEARCH

Investigation on Solid Particle Erosion Performance of Aluminum Alloy Materials for Leading-Edge Slat

Ali İhsan Budur[a], İsmail Özen[b], Bülent Öztürk[c,*], Hasan Gedikli[b]

[a]*Arsin Vocational School, Karadeniz Technical University, 61900, Trabzon, Turkey,*
[b]*Department of Mechanical Engineering, Karadeniz Technical University, 61080, Trabzon, Turkey,*
[c]*Department of Metallurgical and Materials Engineering, Karadeniz Technical University, 61080, Trabzon, Turkey.*

Keywords:

Solid particle erosion
Leading-edge slat
Aluminum alloys
Computational fluid dynamics
Erosion rate

* Corresponding author:

Bülent Öztürk
E-mail: bozturk@ktu.edu.tr

Received: 1 August 2023
Revised: 23 October 2023
Accepted: 18 November 2023

A B S T R A C T

This study aims to characterize solid particle erosion behaviors of three different aluminum alloys (AA2024-T351, AA6061-T651, and AA7075-T651) and reveal their erosion performances on leading-edge slat of airplane wings. Solid particle erosion tests were conducted using silicon carbide erodent particles under the conditions of six different impingement angles (20°-90°) and four different impact velocities (70-192 m/s). The erosion simulations of a leading-edge slat of the aforementioned aluminum alloys were numerically simulated at four different rotation angles (0°-15°) for three different impact velocities (130-250 m/s). A commercial ANSYS Fluent software using the Euler-Lagrange equation and an experimental data-based erosion model was used for the erosion simulations. The experimental results showed that the erosion rate increases with increasing impact velocity and the maximum erosion rate is obtained at the impingement angle of 30° which reflects the ductile manner. Of the three aluminum alloys, the AA6061-T651 exhibited the worst erosion behavior followed by the AA2024-T351 sample, whereas the AA7075-T651 had the best erosion resistance. The numerical results indicated that the erosion rate values of slat surfaces made up of three different aluminum alloys showed a slight increase after a slat rotation angle of 5°.

© 2024 Published by Faculty of Engineering

1. INTRODUCTION

Solid particle erosion is described as taking away material from a target surface owing to the impingement of fast-moving erodent particles on its surface. The amount of erosion and erosion rate is affected by several interrelated factors. The factors contain the properties of the target material (mechanical strength, hardness, surface morphology, microstructure, etc.) and erodent particles (size, shape, hardness, etc.) as well as test conditions. The test conditions include the impact velocity and angle, temperature, erodent flux, etc. [1–6].

Solid particle erosion is a quite common type of wear and the effects have been identified for a long time. The material removal caused by erosion results in an increment in repair and replacement costs, and a decrease of their

lifetime. The damage caused by erosion is confronted in various industries such as aerospace, petrochemical, natural gas, metallurgy, and power generation [7]. Thus far, many authors have investigated the solid particle erosion experimentally and/or numerically in complex curved surface parts used in these industries such as helicopter rotor blades, gas turbine engine compressor/turbine blades, pipe elbows and valves, and leading-edge slats, etc. [8–15].

When a helicopter flies in dust/desert environments, especially low to the ground, the rotor blades are often exposed to solid particle erosion. In this regard, Pepi et al. [16] studied the effects of erosion test parameters on helicopter rotor blades made up of different materials. Another group of researchers has determined numerically the erosion behaviors on helicopter rotor blades coated with various materials using different particle impingement velocities and attack angles [8]. A similar study by Özen and Gedikli [17] investigated experimentally and numerically the solid particle erosion behaviors of helicopter rotor blades covered with Ti-6Al-4V, SS304, Al6061-T6, and Ni materials. Yao et al. [18] used the ANSYS-Fluent software to study the solid particle erosion wear behavior of rotor blades made up of Ti alloy at different rotational speeds and particle flow rates. On the other hand, it has been numerically demonstrated in another study that erosion protection coatings can cause a reduction in the aerodynamic efficiency of the rotor [19].

The erosive wear behavior of gas turbine compressor blades was investigated in many studies [20–22]. Li et al. [23] numerically investigated the erosion behavior of compressor blades caused by the gas-solid flow using the Finnie model [24]. It was observed that wear areas were formed in different regions of the blade surface. Cao et al. [25] analyzed the effect on solid particle erosion of the valve governing mode for nozzles of a large-capacity steam turbine. In another study, Cao et al. [26] numerically studied the effect on the safety and efficiency of solid particle erosion for different notched types of ultra-supercritical steam turbines. Alqallaf and Teixeira [27] conducted numerical simulations using CFD software to determine the solid particle erosion patterns on the compressor blades of turbomachinery. They confirmed that erosion leads to serious reductions in performance parameters such as pressure ratio (PR) and isentropic efficiency (η_{is}).

Slats are aerodynamic surfaces used to adjust the angle of attack on fixed-wing aircraft and are mounted at the leading edge of the wings. As they are extended or retracted, they increase or decrease the surface area of the wing, which results in increasing lift and delaying a stall. The 2XXX, 6XXX, and 7XXX series aluminum alloys are commonly used in aerospace applications [28]. The aluminum-based alloys used in leading edges are typically made up of the 2XXX series and AA2024 alloy is commonly used in the leading edges slats. In the literature, there is almost no assessment of the solid particle erosion of leading-edge slats. However, limited knowledge is about rain erosion. The purpose of the study is therefore to research the solid particle erosion behaviors of leading-edge slats on airplane wings. In accordance with this purpose, three different aluminum alloys, namely, AA2024-T351, AA6061-T651, and AA7075-T651 were chosen as slat materials and the erosive wear of the aforementioned materials was studied experimentally and numerically.

2. EXPERIMENTAL PROCEDURE

The experiments were conducted to assess the erosion wear performance of samples made up of three different aluminum alloys under the conditions of different impact velocities and different impingement angles. The details of the test samples and the erosion wear test apparatus are given below.

2.1 Samples

The test samples were cut from the aluminum plates. The samples with a thickness of 5 mm have a rectangular and square shape with dimensions of 90 mm × 30 mm and 30 mm × 30 mm based on the impingement angle. To eliminate the effect of surface conditions, all test samples were polished with emery paper (Grade No.: 800-1500) and cleaned before the erosion test. The material features of the aluminum alloys used are summarized in Table 1. In the erosion test, silicon carbide (SiC) particles having sizes between 106-150 μm were used as the erodent.

Table 1. Material properties of aluminum alloys.

Material	Density (kg/m³)	Hardness (HB)	Yield strength (MPa)	Tensile strength (MPa)	Elongation (%)
AA2024-T351	2780	120	315	458	19
AA6061-T651	2700	95	298	338	17.5
AA7075-T651	2810	145	510	578	13

2.2 Erosion wear test setup

In order to characterize the solid particle erosion behavior of specimens with three different Al alloy materials, direct particle impact testing was implemented on the specimens. Fig. 1 displays the test setup used for the erosion experiments. The erosion tests can be performed at different velocities and impingement angles in the erosion test rig at room temperature.

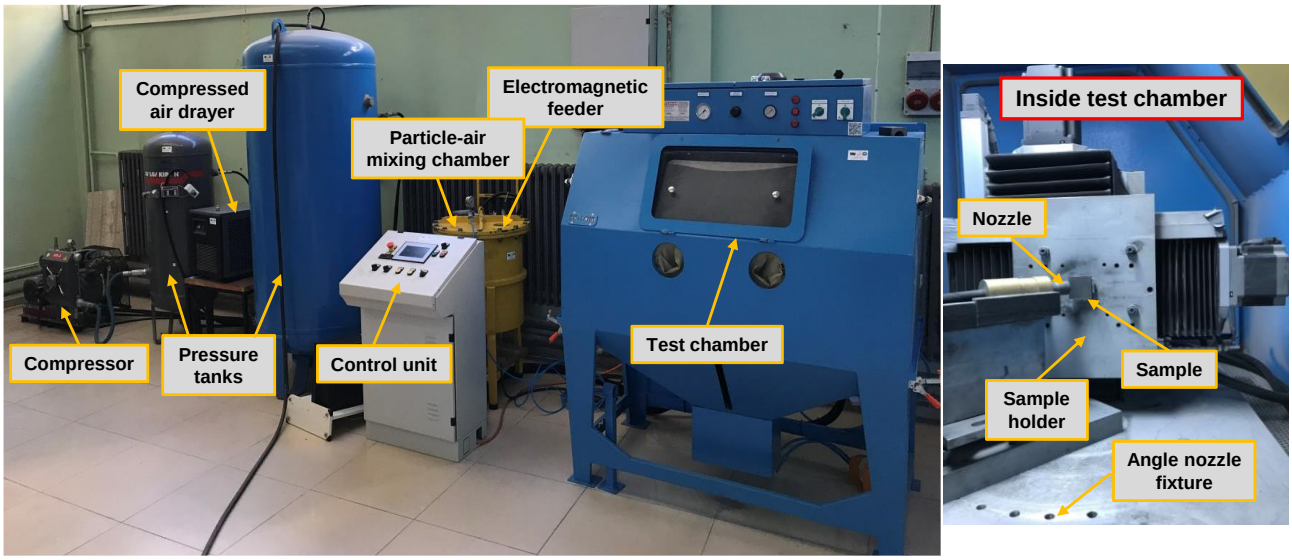

Fig. 1. The solid particle erosion test setup.

During the test, the pressurized air is dried in a drying unit and passed to the mixing chamber. In mixing chamber, the air is blended with the erodent particles. The mass flow rate of the particles is adjusted by an electromagnetic feeder and sent to the test chamber through a hose. In the test chamber, the erodent particles collide with the test sample by accelerating via a nozzle with a throttle diameter of 3.2 mm. ASTM G76 [29] standard was utilized for the solid particle erosion tests. The distance from the nozzle to the sample is set to 10 mm. The particle impact velocity was measured as a function of pressure

using the double-disc technique. The mass flow rate (feed rate) of the particles throughout the tests was kept constant at 2.5 g/min with an accuracy of ±0.2.

To determine parameters involved in the erosion equation used for CFD-based erosion simulations of the leading-edge slat, the erosion experiments of the Al alloy specimens were realized in two main modes. First includes the constant impact velocity of 114 m/s and the different impingement angles i.e., 20°, 30°, 45°, 60°, 75° and 90°. The second addresses the different the impact velocities of 70, 114, 165, and 192 m/s and the impingement angles of 30° and 90°. The erosion tests were repeated three times under the same conditions to enhance the reliability of the experiment results.

The volumetric erosion rate (W_{er}) of the samples during the tests was calculated using the following formula:

$$W_{er} = (\Delta W_s / \Delta W_{ep}) / \rho_s \quad (1)$$

Where ρ_s is sample material density, ΔW_s is the sample weight loss, and ΔW_{ep} is the total weight of the erodent particles (testing time × erodent mass flow rate) used.

The micrographs of worn surfaces of the test specimens were observed using a scanning electron microscope (Zeiss Evo LS10) to characterize the possible wear mechanisms.

2.3 Numerical procedure

2.3.1 Erosion analysis

In this work, numerical analysis of leading-edge slats on airplane wings was carried out using the commercial ANSYS Fluent 16.0 software, which is based on computational fluid dynamics (CFD). This software uses a discrete phase model (DPM) with the Eulerian-Lagrangian method. The erosion analysis is composed of three steps. The three main steps of an overall approach to reveal the erosion behavior of a wished geometry and flow state are flow modeling, particle tracking, and erosion prediction [30]. Flow analysis, the impact velocity, and the impingement angle can be predicted from simplified models or determined more truly by CFD simulations. The following are the details of the numerical procedure.

(1) Flow modeling

The Eulerian-Lagrangian method is used to simulate the particle flow. The fluid flow solution is obtained from the solution of the Reynolds averaged Navier-Stokes equations depending on the principle of conservation of momentum and energy. The continuity and momentum conservation equations are given respectively in equations (2) and (3) [31].

$$\frac{\partial \rho}{\partial t} + \frac{\partial}{\partial x_i}(\rho u_i) = 0 \tag{2}$$

$$\frac{\partial}{\partial t}(\rho u_i) + \frac{\partial}{\partial x_j}(\rho u_i u_j) = -\frac{\partial p}{\partial x_i} + \frac{\partial}{\partial x_j}\left[\mu\left(\frac{\partial u_i}{\partial x_j} + \frac{\partial u_j}{\partial x_i} - \frac{2}{3}\delta_{ij}\frac{\partial u_l}{\partial x_l}\right)\right] + \frac{\partial}{\partial x_j}\left(-\rho\overline{u_i' u_j'}\right) \tag{3}$$

where u, p, μ, and ρ represent the velocity, pressure, dynamic viscosity, and density of the fluid, respectively. δ_{ij} is the Kronecker-Delta operator and $\left(-\rho\overline{u_i' u_j'}\right)$ is known as the Reynolds stress tensor.

(2) Particle tracking

Particle tracking was realized in FLUENT by using the discrete phase model (DPM). With DPM, the trajectory of the particles is determined using the Euler-Lagrangian framework. The particle trajectory is calculated using the following formula:

$$\frac{dV_P}{dt} = F_D(U - V_P) + \frac{g(\rho_p - \rho)}{\rho_p} \tag{4}$$

where V_P and U are the erodent particle velocity and the average fluid velocity, respectively. While ρ_P and ρ are the erodent particle and fluid densities, F_D and g are the particle drag force and gravitational acceleration, respectively. F_D is defined as the following:

$$F_D = \left(\frac{18\mu}{\rho_P {d_p}^2}\right)\frac{C_D Re_{sph}}{24} \tag{5}$$

where d_p is the diameter of the erodent particle, Re_{sph} is the Reynolds number for the spherical particle, and C_D is the particle drag coefficient [32]. The equations related to Re_{sph} and C_D are given in equations (6) and (7), respectively.

$$Re_{sph} = \frac{\rho_P d_P (V_P - U)}{\mu} \tag{6}$$

$$C_D = \frac{24}{Re_{sph}}\left(1 + b_1 {Re_{sph}}^{b_2}\right) + \frac{b_3 Re_{sph}}{b_4 + Re_{sph}} \tag{7}$$

$$b_1 = e^{(2.3288 - 6.4581\emptyset + 2.4486\emptyset^2)} \tag{7a}$$

$$b_2 = 0.0964 + 0.5565\emptyset \tag{7b}$$

$$b_3 = e^{(4.905 - 13.8944\emptyset + 18.4222\emptyset^2 - 10.2599\emptyset^3)} \tag{7c}$$

$$b_4 = e^{(1.4681 + 12.2584\emptyset - 20.7322\emptyset^2 + 15.8855\emptyset^3)} \tag{7d}$$

The particle shape factor:

$$\emptyset = \frac{s}{S} \tag{7e}$$

where s and S are spherical and actual surface areas of the particle, respectively. In the erosion analysis, the non-spherical drag law was utilized. The particle shape factor was taken as 0.7 from the reference [33].

(3) Erosion prediction

There have been many empirical erosion equations to determine the erosion rate of materials in the literature [34–37]. Any erosion rate equation is usually utilized to convert erodent particle impingements to erosion damage. The precision of the erosion equation has also a crucial importance that identifies the reliability of estimated erosion. Most of these equations have been derived from the erosion test and curve fitting approach limiting their applicability to the experimental conditions. For the calculation of the erosion rate in the numerical analysis, an empirical erosion equation was developed using the DNV erosion model [36]. The DNV erosion model is specified as:

$$E = K.{V_P}^n.F(\theta) \tag{8}$$

where K and n are the material constants, V_P is the particle impact velocity and $F(\theta)$ is the function constant with respect to the impingement angle.

The K and n constants can be calculated by using Equations (9) and (10), respectively. These constants were determined by using the erosion data obtained at four different impact velocities (70, 114, 165, and 192 m/s) for the impingement angle of 90°. The values are listed in Table 2.

$$K = \frac{1}{N}\sum_{i}^{N}\frac{E(V_{P,i})}{{V_{P,i}}^n} \tag{9}$$

$$n = \frac{1}{N-1}\sum_{i}^{N-1}\frac{\frac{E_{90}(V_{P,i+1})}{E_{90}(V_{P,i})}}{ln\left[\frac{V_{P,i+1}}{V_{P,i}}\right]} \tag{10}$$

Table 2. K and n constants calculated for the three different aluminum alloys.

Material	K	n
AA2024-T351	1.038×10^{-6}	2.961
AA6061-T651	7.114×10^{-7}	3.051
AA7075-T651	1.816×10^{-6}	2.834

The function constant $F(\theta)$ given in equation (11) can be stated as a function of the impingement angle with respect to radian ($0 \le \theta \le \pi/2$).

$$F(\theta) = C_1\theta + C_2\theta^2 + C_3\theta^3 + C_4\theta^4 + C_5\theta^5 + C_6\theta^6 + C_7\theta^7 \tag{11}$$

The C_1-C_7 are the function constant coefficients calculated using the erosion results obtained at different impingement angles (20°, 30°, 45°, 60°, 75° and 90°) for the impact velocity of 114 m/s. The θ is the erodent particle impingement angle. The C_1-C_7 constants obtained for the test samples are given in Table 3.

Table 3. C1-C7 coefficients calculated for the three different aluminum alloys.

Material	C_1	C_2	C_3	C_4	C_5	C_6	C_7
AA2024-T351	-2.126	43.080	-143.608	219.188	-175.291	71.139	-11.557
AA6061-T651	-1.920	41.506	-139.260	213.508	-171.447	69.837	-11.383
AA7075-T651	-3.482	51.557	-164.503	245.449	-193.435	77.754	-12.555

During movement throughout the flow field, the erodent particles hit the target surface and rebound back to the flow medium. In the current study, the rebound model suggested by researchers [38] was utilized for the erodent particle tracing calculations after the collision. In the model, normal (e_n) and tangential (e_t) coefficients of restitution are defined as polynomials depending on the impingement angle ($0 \le \theta \le \pi/2$) in equations (12) and (13), respectively.

$$e_n = 0.993 - 1.76\theta + 1.56\theta^2 - 0.49\theta^3 \tag{12}$$

$$e_t = 0.988 - 1.66\theta + 2.11\theta^2 - 0.67\theta^3 \tag{13}$$

In order to calculate the removal rate on the slat surface, equation (14) recommended by Mansouri et al. [39] was used in the erosion simulations. The removal rate or thickness loss rate can be expressed as time-dependent material quantity removed from the slat surface due to the particle impact.

$$\Delta\dot{h}_l = \frac{(e_r)_i.\dot{m}_i}{\rho_w A_i} \tag{14}$$

where $(e_r)_i$ is the erosion rate at any cell face; ρ_w is the material density; A_i is the face area for any cell and $\dot{m}_i$ is the particle mass flow rate at any cell.

Accretion rate ($R_{accretion}$) can be defined as the deposition rate on the cell faces of particles striking the surface [31]. It is described as:

$$R_{accretion} = \sum_{i=1}^{N_{particles}} \frac{\dot{m}_i}{A_i} \quad (15)$$

2.3.2 CFD based erosion verification model

In this section, a CFD verification model for solid particle erosion tests was established to validate the accuracy of erosion results on the slat surfaces. Fig. 2 depicts the boundary conditions and the optimal mesh structure of the CFD based verification model. 527660 nodes and 496398 hexagonal elements were utilized to mesh the flow domain and the sample surface in the model. To obtain more accurate results, a fined mesh structure was generated in the region near the sample. The erodent particles were homogeneously injected into the fluid inside the flow domain via a nozzle like in the experimental setup. Inlet velocities of the particle and air were defined as equal to the impact velocity.

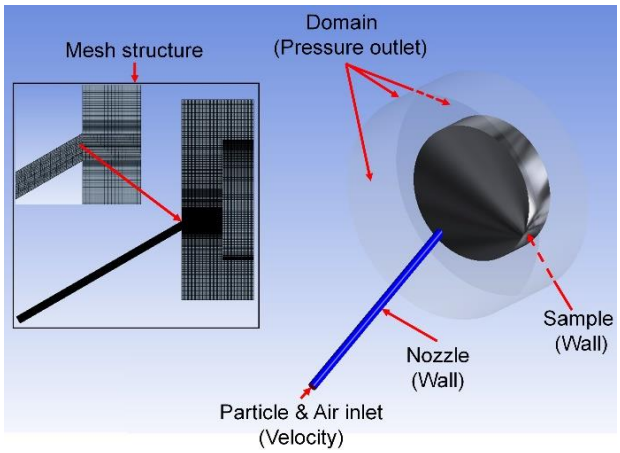

Fig. 2. CFD verification model of solid particle erosion tests.

The erodent particle flux was set to 2.5 gr/min as measured in the experiments. As the boundary conditions, the front face of the sample was chosen as a "Wall". The erosion calculations were applied to this face. The surface in which the erodent particles left the flow domain was selected as the "Pressure Outlet". The erosion analyses were performed both in the conditions of four different impact velocities at the 90° impingement angle and six different aforesaid impingement angles at the impact velocity of 114 m/s. In the analyses, non-spherical drag law was preferred. The erodent particle shape factor was chosen as 0.7 and accuracy control was set to 1×10^{-5}.

2.3.3 CFD-based erosion model for the leading-edge slat geometry

The geometric details of a leading-edge slat and the particle impingement angle and rotation angle details on its target surface are illustrated in Fig. 3 (a, b). The rotation angle of the slat (ϕ) is described as the angle between the tangent line and the reference line of the slat surface. The impingement angle (θ) is expressed as the angle between the particle track and the tangent line of the slat surface.

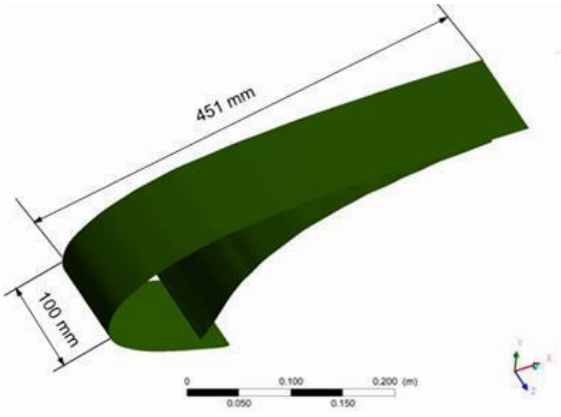

(a)

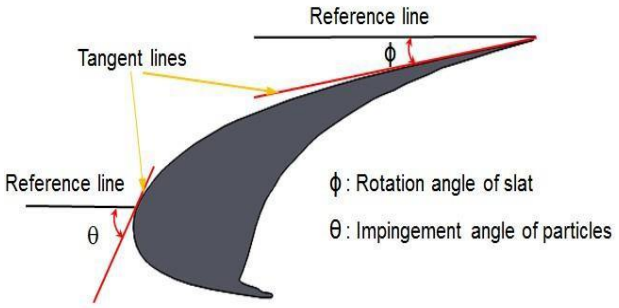

(b)

Fig. 3. (a) Geometric details and, (b) schematic diagram of the studied leading-edge slat.

Fig. 4 (a, b) presents the CFD-based erosion model with mesh structures generated for the slat geometry. As the boundary conditions, no-slip wall boundary condition was defined for slat surfaces and other surfaces of the domain except for inlet and outlet surfaces. For the entry to the domain and out of the domain, velocity inlet and pressure outlet boundary definitions were made respectively. Initial velocities of the erodent particles and the air entering the flow domain were defined as normal to the inlet faces. The air-particle mixture in the flow medium was accepted as homogeneous. The CFD-based erosion analyses for the slat geometry were

performed at three different impact velocities (130, 192, and 250 m/s) and four different rotation angles of the slat (0°, 5°,10°, and 15°). The erosion rate of metallic surfaces under the same particle feed rate conditions indicates a slight variation for bigger particle sizes than 150 µm as reported in reference [17]. Therefore, the average diameter of SiC erodent particles was chosen as 150 µm in the erosion simulations. The mass flow rate in the domain inlet side of the erodent particles was defined as 5.8 g/cm^2 per minute. This value was calculated according to the nozzle outlet diameter of 7.4 mm and particle feed rate of 2.5 g/min involved in the erosion experiments. Inlet velocities of the air and particles were taken equal to the selected impact velocities (130, 192, and 250 m/s).

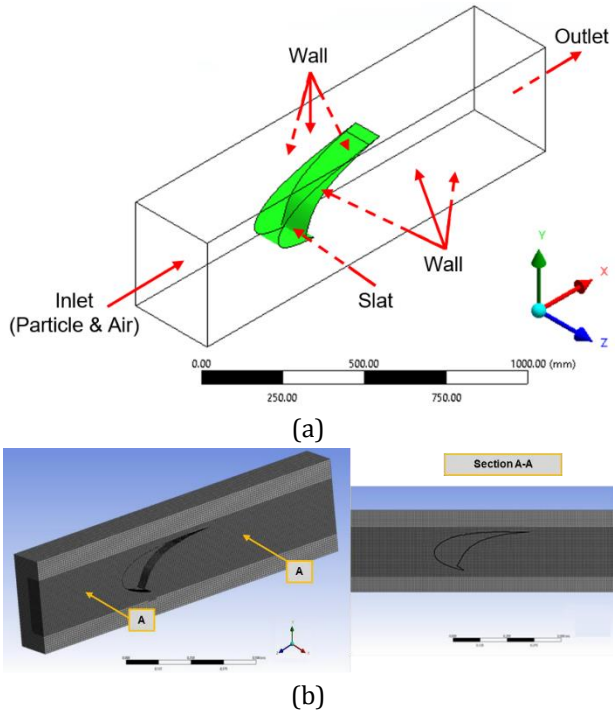

Fig. 4. (a) Boundary conditions and, (b) mesh structure of the leading-edge slat for CFD.

In terms of flow modeling, the mesh structure used, especially in the near-wall zones, influences the near-wall flow area. A fined mesh used near the slat walls can solve more accurately the near wall flows with the boundary layer sufficiently resolved [40,41]. Therefore, a mesh refinement process was applied to obtain a more accurate result at the surfaces near the leading-edge slat (see Fig. 4 (b)). An enhanced wall approach was used to run the erosion analyses. It presents a hybrid near-wall treatment based on near-wall grid resolution. This near-wall approach ensures maximum flexibility in conforming to the alteration of near-wall grid resolution while providing an efficiently precise flow field [42]. The grid independence was validated by the maximum removal rate values obtained from the models with different slat rotation angles to decrease the effect of grid number on computation accuracy. Three different mesh structures were adopted to provide grid independence for the models.

The results of the maximum removal rate and grid number based on the rotation angle of the slat for the impingement velocity of 192 m/s are given in Table 4. As seen in Table 4, according to the results of CFD-based erosion analyses, the maximum removal rate values ignorantly varied until the grid number increased to 5,951,189, 7,190,130, 4,547,625, and 4,626,962 for the models with rotation angles of 0°, 5°, 10° and 15°, respectively. In order to decrease the computation time and develop the calculation accuracy, erosion simulations were carried out with the models of these grid numbers. Hexagonal elements between 4.5 and 7.2 million were used in the erosion models based on the rotation angles of the slat geometry.

Table 4. Relations between maximum removal rate and grid number based on the rotation angle of the slat for the impingement velocity of 192 m/s.

Slat rotation angle (°)	Grid number	Maximum removal rate (µm/s)
0	2,026,652	1.425
	3,412,309	1.435
	5,951,189	1.440
5	2,440,762	1.430
	4,211,371	1.445
	7,190,130	1.435
10	1,648,613	1.450
	3,184,813	1.460
	4,547,625	1.445
15	1,596,850	1.440
	3,181,407	1.477
	4,626,962	1.460

In CFD-based flow analysis, turbulence fluctuations may affect the variables related to the flow field. In the review of the literature, it is observed that the Shear Stress Transport (SST) k-ω turbulence model gives good results for the solution of turbulent flows [17,32]. Therefore, the SST k-ω turbulence model was utilized for the flow simulations. The

fluid flow was modeled as incompressible. The mass and momentum conservation equations were solved for steady-state flow conditions. The motion of solid particles in air pertains to dilute phase air-solid flow. Thus, the one-way coupled dispersed particle approach was adopted. The particle transport model was implemented to define particle motion depending on the Lagrange tracking method [13].

3. RESULTS AND DISCUSSION

3.1 Effect of the impingement angle on the erosion rate

The impingement angle is a crucial parameter influencing the erosion behavior of materials. In general, ductile materials are more susceptible to solid particles during the erosion process. The erosion damage mechanisms of ductile materials take place by micro-cutting, micro-ploughing, and other damage modes. On the other hand, brittle materials exhibit mainly plastic deformation and micro-cracking damage mechanisms [2]. Ductile materials exhibit maximum erosion behavior at low impact angles such as 15°-30°, whereas brittle materials depict maximum erosion behavior at a 90° impingement angle. However, semi-ductile materials indicate maximum erosion behavior at impact angles between 45° and 60° [43].

To find the effect on the impingement angle of the erosion rate of the AA2024-T351, AA6061-T651, and AA7075-T651 alloy samples, the erosion tests were conducted at a constant impact velocity of 114 m/s and varying impingement angles (20°-90°). The results are illustrated in Fig. 5.

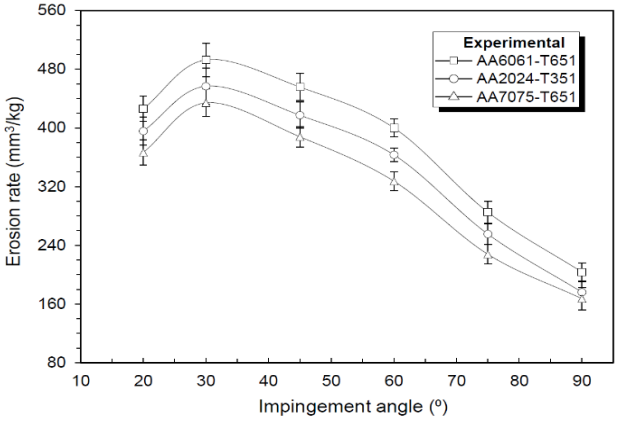

Fig. 5. Effect of the impingement angle on the erosion rate of the aluminum alloy samples at the impact velocity of 114 m/s.

The lowest and highest erosion rates are observed in the AA7075-T651 and AA6061-T651 materials, respectively. This can be ascribed to the higher strength and hardness associated with AA7075-T651 material (see Table 1). It is also clear that the erosion rate of tested samples initially raised with increasing impingement angle, achieving a maximum at a 30° angle after that decreased with increasing impingement angle. The lowest erosion damage occurred at a 90° impingement angle. Therefore, the three studied aluminum alloys exhibited ductile erosion behavior.

3.2 Effect of the impact velocity on the erosion rate

To study the influence of the erodent particle velocity on the erosion rates of the AA2024-T351, AA6061-T651, and AA7075-T651 samples, the experiments were performed at different impingement velocities i.e., 70, 114, 165, and 192 m/s at the impact angles of 30° and 90°. The results obtained are shown in Fig. 6 (a, b).

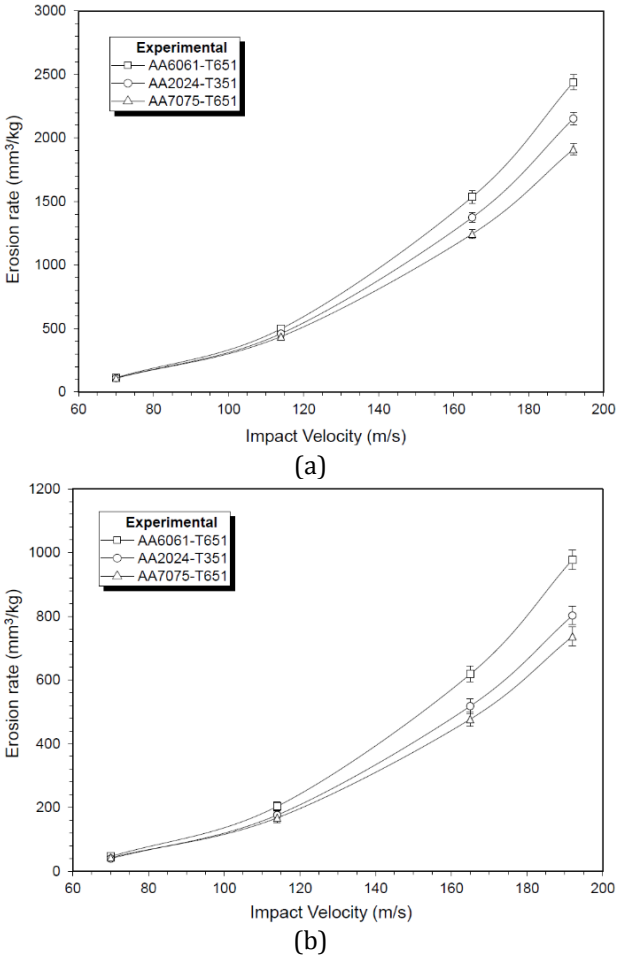

Fig. 6. Effect of the impact velocity on the erosion rate of the aluminum alloy samples at impingement angles of (a) 30° and (b) 90°.

The erosion rates of the samples are seen gradually increasing with increasing impact velocities at both angle values. The AA7075-T651 alloy sample showed the best erosion resistance while the AA6061-T651 material displayed the worst wear resistance. The erosion rate values of the AA6061-T651 sample for an impingement angle of 30° were determined as 112.23 mm^3/kg and 2,438.25 mm^3/kg for impact velocities of 70 m/s and 192 m/s, respectively. According to this result, an increment of 174% in the impact velocity resulted in a twentyfold increment in the erosion value obtained. The corresponding values were noted as 46.29 mm^3/kg and 977.78 mm^3/kg for an impingement angle of 90°, respectively. The increment in velocity rises the kinetic energy of the erodent particles, removing a greater amount of material from the target surface. Also, with increasing velocity, the period between impacts decreases and the energy of the abrasive particle increases, leading to higher volumes of material loss [2,44–47].

3.3 Verification of CFD based erosion results

The wear scar images of experimental and CFD based erosion results of AA6061-T651 material at different impingement angles and impact velocity of 114 m/s are presented in Fig. 7. While the wear scars of the AA6061-T651 sample at the lower impingement angles (20°, 30°, and 45°) had an elliptic shape, they converted to a circular shape at the higher impact angles. At the impingement angle of 90°, the wear scar is almost circular in shape. The experimental and CFD based wear scars are in good agreement with each other. The wear scar area decreased with increasing impingement angle.

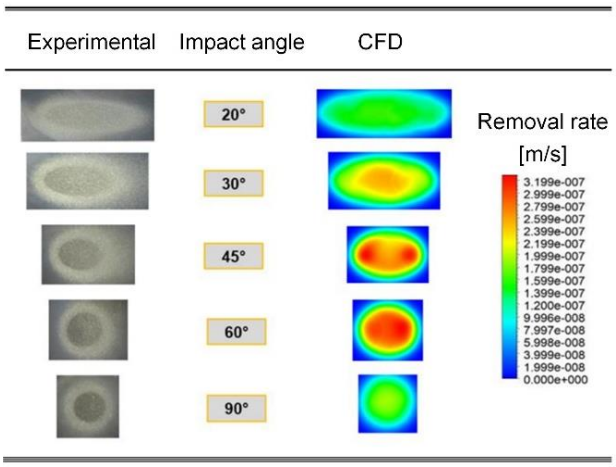

Fig. 7. Comparison of experimental and CFD- based erosion wear scar images obtained for the AA6061-T651 alloy specimen at the impact velocity of 114 m/s.

The experimental and CFD based erosion rate values obtained for AA6061-T651 alloy specimen are listed in Tables 5 and 6. As can be seen from Table, the experimental and CFD based erosion rate values are compatible with each other. At the impact velocity of 114 m/s, the differences between the experimental and CFD based erosion rate results of AA6061-T651 alloy specimen for the impingement angles of 20°, 30°, 45°, 60°, 75° and 90° were approximately obtained as 1%. On the other hand, at the impingement angle of 90°, accuracy of the CFD based erosion results was obtained lower at the higher impact velocities. One possible reason for this situation is that the flow medium had turbulent fluctuations in the higher fluid velocities.

Table 5. Comparison of the experimental and CFD erosion rates at the impact velocity of 114 m/s.

Impact angle (°)	Experimental (mm^3/kg)	CFD (mm^3/kg)	Error %
20	425.93	429.73	0.89
30	492.59	496.99	0.89
45	455.56	459.62	0.89
60	400.01	403.58	0.89
75	285.19	287.81	0.92
90	203.71	205.87	1.06

Table 6. Comparison of the experimental and CFD erosion rates at the impact angle of 90°.

Impact velocity (m/s)	Experimental (mm^3/kg)	CFD (mm^3/kg)	Error %
70	46.29	46.24	0.11
114	203.71	205.87	1.06
165	618.52	632.67	2.28
192	977.78	1004.58	2.74

3.4 CFD-based erosion results on the leading-edge slat surface

Numerical simulations were realized to find the erosion rate removal rate and accretion rate distributions on the leading-edge slat surfaces, focusing on the slat rotation angle and the particle impact velocity. Fig. 8 depicts the bar charts of the erosion rate results obtained with CFD simulations on the slat surfaces made up of AA2024-T351, AA6061-T651, and AA7075-T651 materials at different impacts velocities of 130, 192, and 250 m/s for a rotation angle of 0°.

The erosion rate values increased with increasing impact velocity. Their erosion rate values were approximately the same at low impact velocity, however, the differences between the erosion rates went up with an increment of the impact velocity. The erosion rate values at impact velocities of 130, 192, and 250 m/s were found as 420.12, 1,365.15, and 2,940.25 mm³/kg for the AA7075-T651 sample and 490.32, 1,680.23, and 3,780.14 mm³/kg for the AA6061-T651 sample, respectively. Taking into account the results presented in Fig. 8, it is evaluated that the AA7075-T651 alloy sample exhibits the best erosion performance while the AA6061-T651 material exhibits the worst erosion performance.

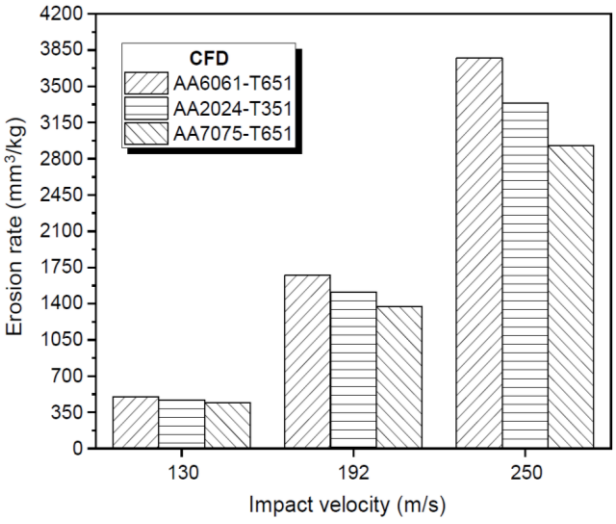

Fig. 8. Variation with the impact velocity of erosion rate on the slat surface for the rotation angle of 0°.

Fig. 9 displays the removal rate distributions obtained with CFD simulations along the slat surface at different impact velocities of 130, 192, and 250 m/s for the rotation angle of 0°. Considering the removal rate scales, the maximum removal rate value on the slat surface of the AA7075-T651 sample is lower than those of the AA2024-T351 and AA6061-T651 samples. The lower removal rate values were obtained at the nose side of the slat surface where the erodent particles hit at the impingement angle of 90°. However, the removal rates on the surfaces above the nose side were obtained higher. The possible reason for this is that the particles hit these surfaces with an impingement angle between 30° and 60°, which indicates more severe erosion damage for ductile materials. It can also be seen from the scales that the removal rate values increased clearly at the higher impact velocities.

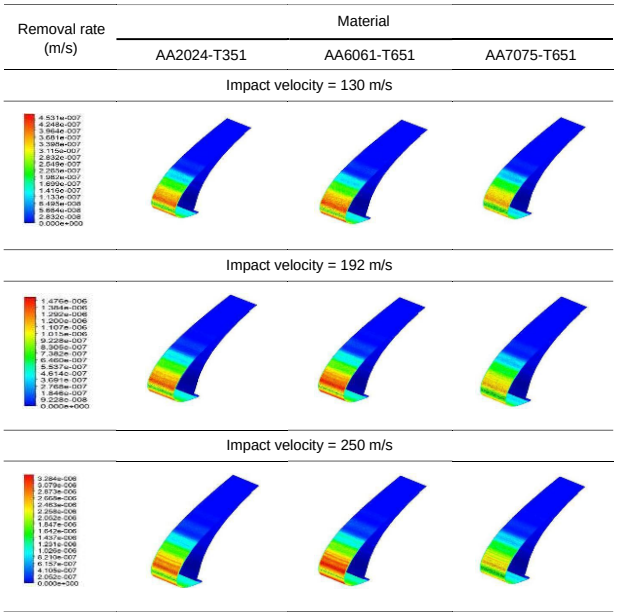

Fig. 9. Removal rate distributions predicted by CFD analysis at different impact velocities for three studied aluminum alloys (rotation angle of the leading-edge slat: 0°).

The CFD accretion rate distributions of the AA2024-T351 material at the rotation angles of 0° and 15° are depicted in Fig. 10. As the mass flow rate of the particles is selected constant, the accretion rate values on the slat surfaces for three studied aluminum alloys were obtained similarly under the conditions of the same slat rotation angles and the particle impact velocities. Therefore, the accretion rate distribution throughout the slat surface is given for only one material (AA2024-T351). The maximum accretion rate was observed at the nose side of the slat where the abrasive particles struck the surface with an impact angle of 90°. In the upper part of the slat surface, the amount of accretion rate decreased as the particles collided with the surface at lower angles. In addition, the accretion rate at the rotation angle of 0° was obtained higher than that of 15°.

Fig. 10 also indicates that an increment in erodent particle velocity has a slight influence on the accretion rate.

Fig. 11 illustrates CFD erosion rate variations according to the rotation angles of the slat surfaces for an impact velocity of 192 m/s. From the figure, it is clear that increasing the rotation angle of the slat had little influence on the erosion rate of the slat surfaces. The erosion rate values of slat surfaces made up of three different aluminum alloys showed a slight increase after a slat rotation angle of 5°. On the other hand, the

solid particle erosion performance of the AA7075-T651 material is better than those of the AA2024-T351 and AA6061-T651 materials.

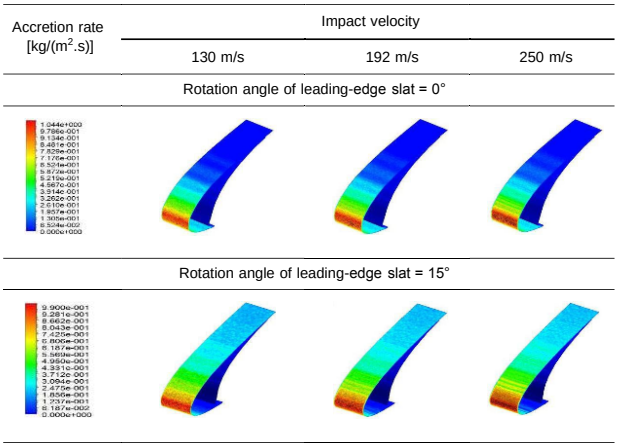

Fig. 10. Accretion rate distributions predicted by CFD analysis at rotation angles of leading-edge slat of 0° and 15° for different impact velocities (material: AA2024-T351).

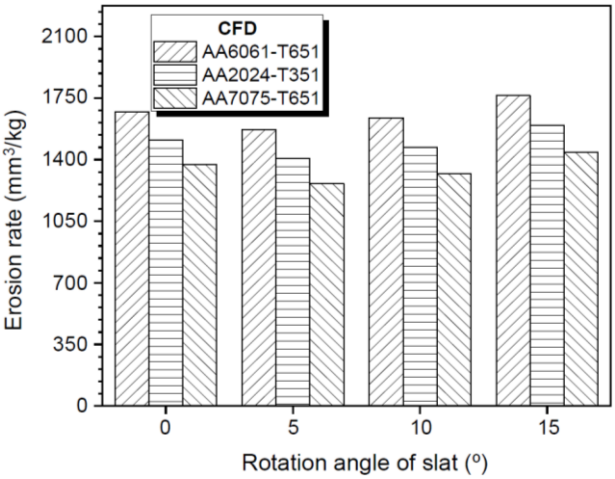

Fig. 11. Variation with rotation angle of erosion rate on the slat surface for the impact velocity of 192 m/s.

Fig. 12 indicates the CFD removal rate distributions obtained at different rotation angles of the slat surfaces for the impact velocity of 192 m/s. The removal rate field of the slat surfaces raised with the increasing rotation angle of the slat. The wear region regardless of the material type expands to the upper surface of the slat.

The variation of the accretion rate based on the slat rotation angle of AA2024-T351 aluminum alloy at the impact velocity of 192 m/s is depicted in Fig. 13. The maximum accretion rate was observed at the nose side of the slat surface. With increasing the rotation angle of the slat, the erodent particles accumulated on the upper surface of the slat.

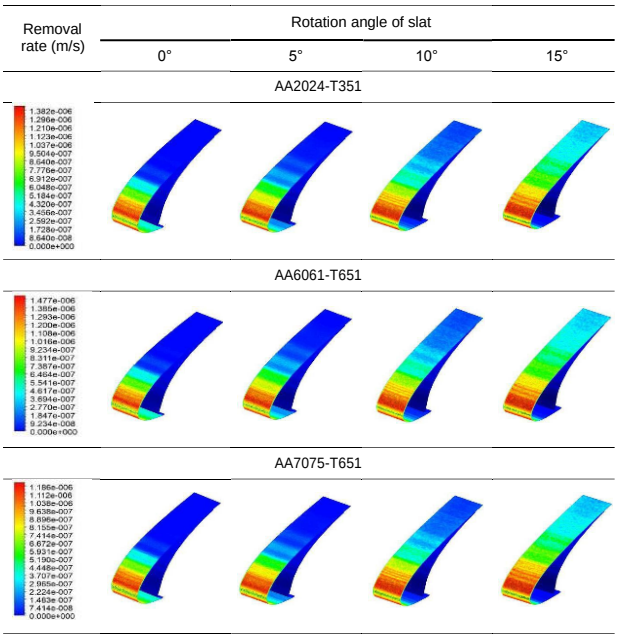

Fig. 12. Removal rate distributions predicted by CFD analysis at different slat rotation angles for three studied aluminum alloys (the impact velocity:192 m/s).

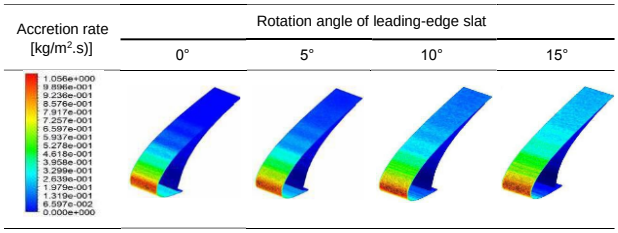

Fig. 13. Accretion rate distributions predicted by CFD analysis at different slat rotation angles for an impact velocity of 192 m/s (material: AA2024-T351).

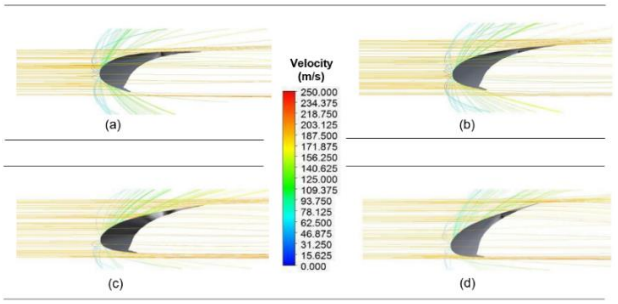

Fig. 14. Variation of the particle trajectory and the impact velocity for different rotation angles of the leading-edge slat of (a) 0°, (b) 5°, (c) 10° and (d) 15°.

Fig 14 shows the variation of particle trajectory and impact velocity at different rotation angles of the slat of 0°, 5°, 10°, and 15°. In the figure, the particle rebound velocities and trajectories around the slat were colored by their velocity magnitude. The particle rebound velocities and trajectories changed depending on the rotation angle and geometry of the leading-edge slat. The erodent particles hit the slat surface and rebounded from the upper and

lower surface of the slat at the rotation angle of 0°. On the other hand, with increasing the rotation angle, most of the erodent particles rebounded from the upper surface of the slat.

3.5 Surface morphology of the eroded samples

The SEM micrographs and the scar images of the worn surfaces of AA2024-T351, AA6061-T651, and AA7075-T651 alloy samples at impingement angles of 30° and 90° were presented in Figs. 15 (a-c) and 16 (a-c), respectively. The shape of the erosion scars of the specimens at the impingement angle of 30° is elliptical. The wear scar converted from an elliptical to a circular shape as the angle is increased to 90°. At the impingement angle of 90°, the wear scar is almost circular in shape. The erosion scar area decreased with increasing impact angle. This can be caused by the impact region and form of the nozzle as observed commonly in other studies [43,48].

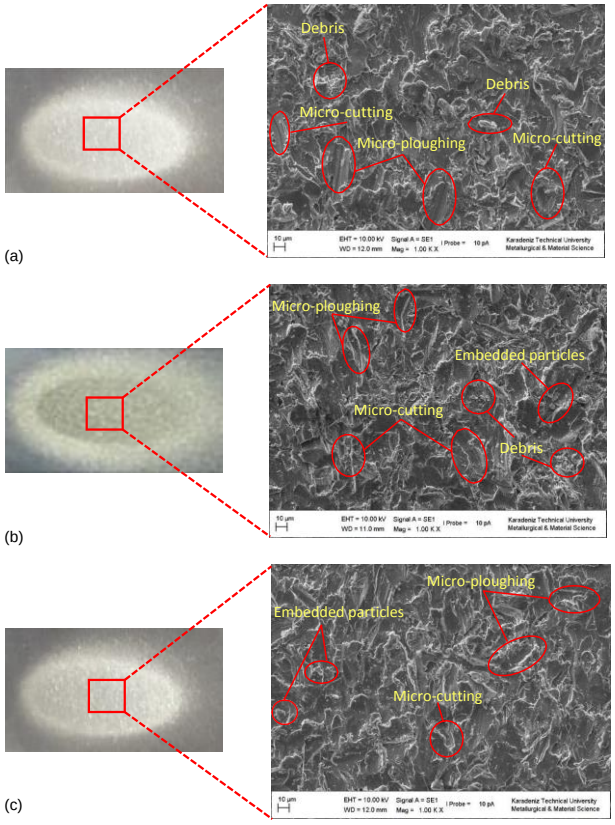

Fig. 15. SEM micrographs of the worn surfaces of (a) AA2024-T351, (b) AA6061-T651 and (c) AA7075-T651 samples at the impact angle of 30° for the impact velocity of 114 m/s.

When the particles strike a surface at grazing angles, cutting damage occurs in the impact zone due to shearing tension. If the particle kinetic energy is high enough, the particles embed to the surface and cause plastic deformation damage. This situation is repeated for the particle bombardments, which continue until a part of the material is removed by scraping from the surface. In the case of the particles hitting the surface at a normal angle, the repetitive impingements lead to plastic deformation which causes embedding to the surface of particles [49]. At the impact angles of 30° and 90°, it is observed that the dominant material removal mechanisms are deep grooving, micro-cutting, and ploughing actions. Normal and shear stresses have crucial effects on the erosion behavior of ductile materials [50,51]. The material loss due to cutting and ploughing (grooves on the surface) mechanisms as seen from Fig. 15 (a-c) is interrelated to the removal of all sample surfaces in the shape of chips by the effect of shearing stresses owing to the erodent material [52]. Some erodent fragments were embedded on the surfaces of the samples. At an impingement angle of 90°, the material detachments are in the form of spalt due to strong normal stress. It is possible to define micro-cutting and micro-ploughing actions, more embedded fragments deposited on the worn surfaces, as shown in Fig. 16 (a-c).

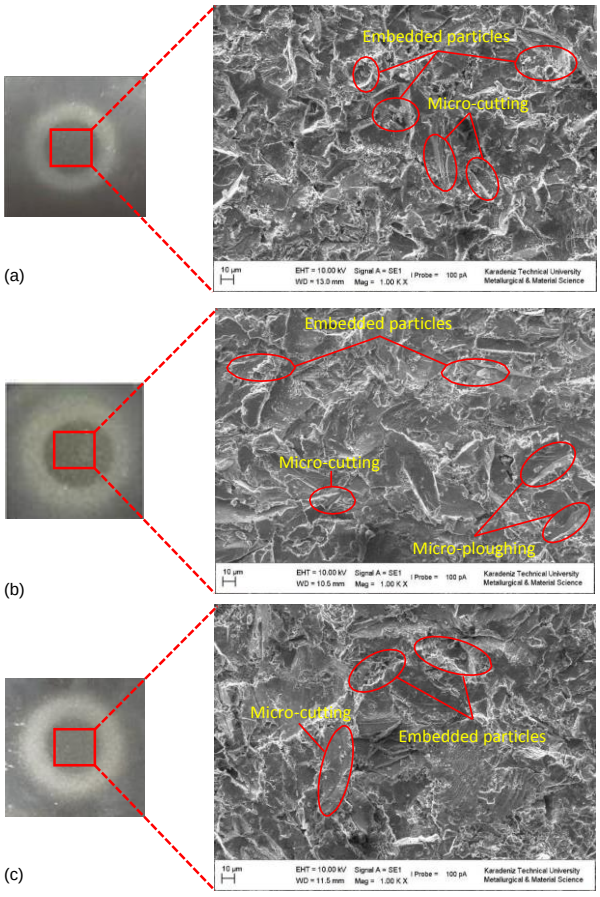

Fig. 16. SEM micrographs of the worn surfaces of (a) AA2024-T351, (b) AA6061-T651 and (c) AA7075-T651 samples at the impact angle of 90° for the impact velocity of 114 m/s.

4. CONCLUSION

This study aimed to reveal the solid particle erosion performances of three different aluminum alloys (AA2024-T351, AA6061-T651, and AA7075-T651) on leading-edge slats of airplane wings. For this purpose, the erosion tests of these aluminum alloys were carried out at different impact angles from 20° to 90° and impingement velocities between 70 - 192 m/s with silicon carbide (SiC) erodent particles. The erosion performance of these materials chosen as the leading-edge slats was numerically examined under the conditions of different rotation angles of the slat (0°-15°) and three impact velocities (130, 192, and 250 m/s). Numerical analysis of the slats was performed by using the ANSYS Fluent CFD package. Based on the current investigation, the following conclusions can be drawn:

1. AA7075-T651 sample showed better erosion resistance than other tested samples.
2. AA2024-T351, AA6061-T651, and AA7075-T651 samples exhibited maximum erosion rate at an impact angle of 30°. Moreover, the erosion rates of all the samples raised with increasing impact velocity.
3. The erosion rate values of the slat surfaces showed a slight increase after a slat rotation angle of 5°. The maximum accretion rate values were obtained at the nose side of the slat.
4. Rebound velocities and trajectories of the erodent particles changed remarkably depending on the rotation angle and geometry of the leading-edge slat.
5. According to SEM images taken at the impingement angles of 30° and 90°, the dominant material removal mechanisms were deep grooving, micro-cutting, and micro-ploughing.

REFERENCES

[1] E. Akbarzadeh, E. Elsaadawy, A. Sherik, J. K. Spelt, and M. Papini, "The solid particle erosion of 12 metals using magnetite erodent," *Wear*, vol. 282–283, pp. 40–51, Apr. 2012, doi: 10.1016/j.wear.2012.01.021.

[2] M. A. Chowdhury, U. K. Debnath, D. M. Nuruzzaman, and Md. M. Islam, "Experimental analysis of aluminum alloy under solid particle erosion process," *Proceedings of the Institution of Mechanical Engineers, Part J: Journal of Engineering Tribology*, vol. 230, no. 12, pp. 1516–1541, Aug. 2016, doi: 10.1177/1350650116639466.

[3] K. Shimizu, X. Yaer, and S. Araya, "Solid particle erosion and mechanical properties of stainless steels at elevated temperature," *Wear*, vol. 271, no. 9–10, pp. 1357–1364, Jul. 2011, doi: 10.1016/j.wear.2010.12.038.

[4] A. P. Harsha and D. K. Bhaskar, "Solid particle erosion behaviour of ferrous and non-ferrous materials and correlation of erosion data with erosion models," *Materials in Engineering*, vol. 29, no. 9, pp. 1745–1754, Oct. 2008, doi: 10.1016/j.matdes.2008.03.016.

[5] M. Buszko and A. Krella, "An influence of factors of flow condition, particle and material properties on slurry erosion resistance," *Advances in Materials Sciences*, vol. 19, no. 2, pp. 28–53, Jun. 2019, doi: 10.2478/adms-2019-0010.

[6] G. R. Desale, B. K. Gandhi, and S. C. Jain, "Particle size effects on the slurry erosion of aluminium alloy (AA 6063)," *Wear*, vol. 266, no. 11–12, pp. 1066–1071, May 2009, doi: 10.1016/j.wear.2009.01.002.

[7] Arabnejad, H., Mansouri, A., Shirazi, S.A., McLaury, B.S., "Evaluation of Solid Particle Erosion Equations and Models for Oil and Gas Industry Applications," *SPE Annual Technical Conference and Exhibition,* pp. 3603–3621, Sep. 2015, doi: 10.2118/174987-MS.

[8] X. Bai, Y. Yao, Z. Han, J. Zhang, and S. Zhang, "Study of solid particle erosion on helicopter rotor blades surfaces," *Applied Sciences*, vol. 10, no. 3, p. 977, Feb. 2020, doi: 10.3390/app10030977.

[9] H. Pouraria, F. Darihaki, K. H. Park, S. A. Shirazi, and Y. Seo, "CFD modelling of the influence of particle loading on erosion using dense discrete particle model," *Wear*, vol. 460–461, p. 203450, Nov. 2020, doi: 10.1016/j.wear.2020.203450.

[10] X. Chen, B. S. McLaury, and S. A. Shirazi, "Numerical and experimental investigation of the relative erosion severity between plugged tees and elbows in dilute gas/solid two-phase flow," *Wear*, vol. 261, no. 7–8, pp. 715–729, Oct. 2006, doi: 10.1016/j.wear.2006.01.022.

[11] R. E. Vieira, A. Mansouri, B. S. McLaury, and S. A. Shirazi, "Experimental and computational study of erosion in elbows due to sand particles in air flow," *Powder Technology*, vol. 288, pp. 339–353, Jan. 2016, doi: 10.1016/j.powtec.2015.11.028.

[12] L. Xu, Q. Zhang, J. Zheng, and Y. Zhao, "Numerical prediction of erosion in elbow based on CFD-DEM simulation," *Powder Technology*, vol. 302, pp. 236–246, Nov. 2016, doi: 10.1016/j.powtec.2016.08.050.

[13] Z. Mazur, R. Campos-Amezcua, G. Urquiza, and A. García-Gutiérrez, "Numerical 3D simulation of the erosion due to solid particle impact in the main stop valve of a steam turbine," *Applied Thermal Engineering*, vol. 24, no. 13, pp. 1877–1891, Sep. 2004, doi: 10.1016/j.applthermaleng.2004.01.001.

[14] D. Li-Ping, Y. Mao-Zheng, and Y. Dai, "Nozzle passage aerodynamic design to reduce solid particle erosion of a supercritical steam turbine control stage," *Wear*, vol. 262, no. 1–2, pp. 104–111, Jan. 2007, doi: 10.1016/j.wear.2006.04.010.

[15] İ. Özen, H. Gedikli, and B. Öztürk, "Improvement of solid particle erosion resistance of helicopter rotor blade with hybrid composite shield," *Engineering Failure Analysis*, vol. 121, p. 105175, Mar. 2021, doi: 10.1016/j.engfailanal.2020.105175.

[16] M. Pepi, R. Squillacioti, L. Pfledderer, and A. W. Phelps, "Solid particle erosion testing of helicopter rotor blade materials," *Journal of Failure Analysis and Prevention*, vol. 12, no. 1, pp. 96–108, Dec. 2011, doi: 10.1007/s11668-011-9531-3.

[17] İ. Özen and H. Gedikli, "Solid particle erosion on shield surface of a helicopter rotor blade using computational fluid dynamics," *Journal of Aerospace Engineering*, vol. 32, no. 1, Jan. 2019, doi: 10.1061/(asce)as.1943-5525.0000962.

[18] Y. Yao, X. Bai, H. Liu, T. Li, J. Liu, and G. Zhou, "Solid particle erosion area of rotor blades: application on Small-Size unmanned helicopters," *Symmetry*, vol. 13, no. 2, p. 178, Jan. 2021, doi: 10.3390/sym13020178.

[19] M. Calvert and T.-C. Wong, "Aerodynamic impacts of helicopter blade erosion coatings," *30th AIAA Applied Aerodynamics Conference*, Jun. 2012, doi: 10.2514/6.2012-2914.

[20] J. Alqallaf, N. Ali, J. A. Teixeira, and A. Addali, "Solid Particle Erosion Behaviour and Protective Coatings for Gas Turbine Compressor Blades—A Review," *Processes*, vol. 8, no. 8, p. 984, Aug. 2020, doi: 10.3390/pr8080984.

[21] A. Hamed, W. Tabakoff, R. B. Rivir, K. Das, and P. Arora, "Turbine blade surface deterioration by erosion," *Journal of Turbomachinery*, vol. 127, no. 3, pp. 445–452, Mar. 2004, doi: 10.1115/1.1860376.

[22] B. Taherkhani, A. P. Anaraki, J. Kadkhodapour, N. K. Farahani, and H. Tu, "Erosion due to solid particle impact on the turbine blade: experiment and simulation," *Journal of Failure Analysis and Prevention*, vol. 19, no. 6, pp. 1739–1744, Oct. 2019, doi: 10.1007/s11668-019-00775-y.

[23] C. Li, G. Bin, J. Li, and Z. Liu, "Study on the erosive wear of the gas-solid flow of compressor blade in an aero-turboshaft engine based on the Finnie model," *Tribology International*, vol. 163, p. 107197, Nov. 2021, doi: 10.1016/j.triboint.2021.107197.

[24] I. Finnie, "Erosion of surfaces by solid particles," *Wear*, vol. 3, no. 2, pp. 87–103, Mar. 1960, doi: 10.1016/0043-1648(60)90055-7.

[25] L. Cao, S. Liu, Y.-C. Li, and H. Si, "Influence of valve governing mode on solid particle erosion and efficiency in governing stage of steam turbine," *Energy*, vol. 191, p. 116581, Jan. 2020, doi: 10.1016/j.energy.2019.116581.

[26] L. Cao, C. Tu, P. Hu, and S. Liu, "Influence of solid particle erosion (SPE) on safety and economy of steam turbines," *Applied Thermal Engineering*, vol. 150, pp. 552–563, Mar. 2019, doi: 10.1016/j.applthermaleng.2018.12.172.

[27] J. Alqallaf and J. A. Teixeira, "Numerical study of effects of solid particle erosion on compressor and engine performance," *Results in Engineering*, vol. 15, p. 100462, Sep. 2022, doi: 10.1016/j.rineng.2022.100462.

[28] C. Duraipandi, A. M. Khan, J. J. T. Winowlin, N. M. Ghazaly, and P. M. Mashinini, "Solid particle erosion studies of thermally deposited alumina-titania coatings on an aluminum alloy," *International Journal of Minerals, Metallurgy and Materials*, vol. 28, no. 7, pp. 1186–1193, Jul. 2021, doi: 10.1007/s12613-020-2099-8.

[29] *Standard Test Method for Conducting Erosion Tests by Solid Particle Impingement Using Gas Jets*, ASTM G76-07, 2013.

[30] H. Arabnejad, A. Mansouri, S. A. Shirazi, and B. S. McLaury, "Development of mechanistic erosion equation for solid particles," *Wear*, vol. 332–333, pp. 1044–1050, May 2015, doi: 10.1016/j.wear.2015.01.031.

[31] Ansys Fluent Theory Guide. ANSYS Inc, 15317, Canonsburg, 2021, available at: https://dl.cfdexperts.net/cfd_resources/Ansys_Documentation/Fluent/Ansys_Fluent_Theory_Guide.pdf, accessed: 20.11.2023.

[32] A. S. Haider and O. Levenspiel, "Drag coefficient and terminal velocity of spherical and nonspherical particles," *Powder Technology*, vol. 58, no. 1, pp. 63–70, May 1989, doi: 10.1016/0032-5910(89)80008-7.

[33] A. Uzi, Y. Ben-Ami, and A. Levy, "Erosion prediction of industrial conveying pipelines," *Powder Technology*, vol. 309, pp. 49–60, Mar. 2017, doi: 10.1016/j.powtec.2016.12.087.

[34] Y. Zhang, E. P. Reuterfors, B. S. McLaury, S. A. Shirazi, and E. F. Rybicki, "Comparison of computed and measured particle velocities and erosion in water and air flows," *Wear*, vol. 263, no. 1–6, pp. 330–338, Sep. 2007, doi: 10.1016/j.wear.2006.12.048.

[35] Y. Oka, K. Okamura, and T. Yoshida, "Practical estimation of erosion damage caused by solid particle impact," *Wear*, vol. 259, no. 1–6, pp. 95–101, Jul. 2005, doi: 10.1016/j.wear.2005.01.039.

[36] DNV-RP-O501 Managing Sand Production and Erosion Hamburg, 2015, available at: https://www.dnv.com/oilgas/download/dnv-rp-O501-managing-sand-production-and-erosion.html, accessed: 20.11.2023.

[37] A. Mansouri, H. Arabnejad, S. Karimi, S. A. Shirazi, and B. S. McLaury, "Improved CFD modeling and validation of erosion damage due to fine sand particles," *Wear*, vol. 338–339, pp. 339–350, Sep. 2015, doi: 10.1016/j.wear.2015.07.011.

[38] M. E. Taslim, A. Khanicheh, and S. D. Spring, "A numerical study of sand separation applicable to engine inlet particle separator systems," *Journal of the American Helicopter Society*, vol. 54, no. 4, p. 042001, Jan. 2009, doi: 10.4050/jahs.54.042001.

[39] A. Mansouri, H. Arabnejad, S. A. Shirazi, and B. S. McLaury, "A combined CFD/experimental methodology for erosion prediction," *Wear*, vol. 332–333, pp. 1090–1097, May 2015, doi: 10.1016/j.wear.2014.11.025.

[40] Y. Zhang, B. S. McLaury, and S. A. Shirazi, "Improvements of particle Near-Wall velocity and erosion predictions using a commercial CFD code," *Journal of Fluids Engineering-transactions of the Asme*, vol. 131, no. 3, Feb. 2009, doi: 10.1115/1.3077139.

[41] Fard, F.N., McLaury, B., Shirazi, S., "Effect of Cell Size on Particle-Eddy Interaction and Erosion Predictions Using Commercial CFD Software (FLUENT)," *In Proceedings of the American Society of Mechanical Engineers, Fluids Engineering Division (Publication) FEDSM*, vol. 1, pp. 1287–1295, Jul. 2012, doi: 10.1115/FEDSM2012-72294J.

[42] Zhang, B. S. McLaury, and S. A. Shirazi, "Application and experimental validation of a CFD based erosion prediction procedure for jet impingement geometry," *Wear*, vol. 394–395, pp. 11–19, Jan. 2018, doi: 10.1016/j.wear.2017.10.001.

[43] J. R. Laguna-Camacho, E. A. G.-H. M. Vite-Torres, and E. E. Vera-Cárdenas, "Solid particle erosion on different metallic materials," in *InTech eBooks*, 2013. doi: 10.5772/51176.

[44] M. Pethuraj, M. Uthayakumar, S. Rajakarunakaran, and S. Rajesh, "Solid particle erosive behaviour of sillimanite reinforced aluminium metal matrix composites," *Materials Research Express*, vol. 5, no. 6, p. 066514, Jun. 2018, doi: 10.1088/2053-1591/aac8ba.

[45] B. Öztürk, H. Gedikli, and Y. S. Kılıçarslan, "Erosive wear characteristics of E-glass fiber reinforced silica fume and zinc oxide-filled epoxy resin composites," *Polymer Composites*, vol. 41, no. 1, pp. 326–337, Aug. 2019, doi: 10.1002/pc.25372.

[46] M. Yadav, L. A. Kumaraswamidhas, and S. K. Singh, "Investigation of solid particle erosion behavior of Al-Al_2O_3 and Al-ZrO_2 metal matrix composites fabricated through powder metallurgy technique," *Tribology International*, vol. 172, p. 107636, Aug. 2022, doi: 10.1016/j.triboint.2022.107636.

[47] M. A. Chowdhury, N. Hossain, M. Shahin, U. K. Debnath, M. M. Rahman, and M. M. Rahman, "Erosion characteristics of stainless steels under different percentage of SiC- Al_2O_3-Fe_2O_3 solid particles," *Tribology International*, vol. 167, p. 107403, Mar. 2022, doi: 10.1016/j.triboint.2021.107403.

[48] Md. A. Islam, Z. Farhat, and E. M. Ahmed, "Influence of impact angle and velocity on erosion of AISI 1018 steel under jet impingement," *Elsevier eBooks*, 2012, pp. 274–279. doi: 10.1016/b978-0-444-59496-9.50038-2.

[49] H. Meng and K. C. Ludema, "Wear models and predictive equations: their form and content," *Wear*, vol. 181–183, pp. 443–457, Mar. 1995, doi: 10.1016/0043-1648(95)90158-2.

[50] R. Tarodiya and B. K. Gandhi, "Experimental investigation on slurry erosion behavior of 304L steel, grey cast iron, and high chromium white cast iron," *Journal of Tribology*, vol. 141, no. 9, Jun. 2019, doi: 10.1115/1.4043903.

[51] J. R. Laguna-Camacho *et al.*, "Erosion behavior of AISI 6061-T6," *Journal of Surface Engineered Materials and Advanced Technology*, vol. 05, no. 03, pp. 136–146, Jan. 2015, doi: 10.4236/jsemat.2015.53015.

[52] M. A. Chowdhury, U. K. Debnath, D. M. Nuruzzaman, and Md. M. Islam, "Study of erosive surface characterization of copper alloys under different test conditions," *Surfaces and Interfaces*, vol. 9, pp. 245–259, Dec. 2017, doi: 10.1016/j.surfin.2017.10.005.